Low-Frequency Raman Fingerprints of Two-Dimensional Metal Dichalcogenide Layer Stacking Configurations

Alexander A. Puretzky,*,† Liangbo Liang,‡ Xufan Li,† Kai Xiao,† Kai Wang,† Masoud Mahjouri-Samani,† Leonardo Basile,∥ Juan Carlos Idrobo,† Bobby G. Sumpter,†,§ Vincent Meunier,‡ and David B. Geohegan†

†Center for Nanophase Materials Sciences, Oak Ridge National Laboratory, Oak Ridge, Tennessee 37831, United States, ‡Department of Physics, Applied Physics, and Astronomy, Rensselaer Polytechnic Institute, Troy, New York 12180, United States, §Computer Science and Mathematics Division, Oak Ridge National Laboratory, Oak Ridge, Tennessee 37831, United States, and ∥Departamento de Física, Escuela Politécnica Nacional, Quito 170525, Ecuador

ABSTRACT The tunable optoelectronic properties of stacked two-dimensional (2D) crystal monolayers are determined by their stacking orientation, order, and atomic registry. Atomic-resolution Z-contrast scanning transmission electron microscopy (AR-Z-STEM) and electron energy loss spectroscopy (EELS) can be used to determine the exact atomic registration between different layers, in few-layer 2D stacks; however, fast optical characterization techniques are essential for rapid development of the field. Here, using two- and three-layer $MoSe_2$ and WSe_2 crystals synthesized by chemical vapor deposition, we show that the generally unexplored low frequency (LF) Raman modes (<50 cm^{-1}) that originate from interlayer vibrations can serve as fingerprints to characterize not only the number of layers, but also their stacking configurations. *Ab initio* calculations and group theory analysis corroborate the experimental assignments determined by AR-Z-STEM and show that the calculated LF mode fingerprints are related to the 2D crystal symmetries.

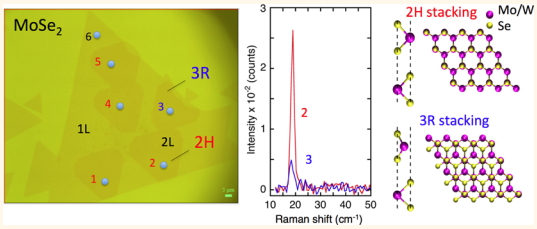

KEYWORDS: two-dimensional materials · transition metal dichalcogenides · low-frequency Raman spectroscopy · stacking configurations · first-principles calculations

Stacking of two-dimensional (2D) van der Waals (vdW) crystals is considered a powerful approach to produce new artificially structured materials[1,2] and heterostructures[3−5] for electronic and optoelectronic applications.[6−8] This approach can generate a variety of structures by combining a number of identical or different 2D layers with varying relative orientations. Characterization of 2D crystals has been largely based on a variety of electron microscopy, atomic force microscopy, and optical spectroscopy methods. Among these, Raman spectroscopy has attracted considerable attention due to its simplicity and ability to provide nondestructive structural information about nanomaterials, as has been conclusively demonstrated for carbon nanotubes[9−11] and graphene.[12−14]

Raman spectroscopy has already been extensively employed to characterize few-layer 2D transition metal dichalcogenides (TMDs).[15] Until now, mainly the intralayer vibrations with relatively large frequencies >100 cm^{-1} have been probed. However, Raman spectral frequencies below ~50 cm^{-1} contain a wealth of information regarding the low-frequency (LF) shear and breathing modes associated with in-plane and out-of-plane interlayer vibrations, respectively. These modes provide the most sensitive measurements of the vdW interactions and coupling between layers in stacked 2D crystals with different numbers of layers and phases. The atomic stacking patterns in few-layer TMDs are similar to those in graphene.[16,17] Studies of LF modes in TMDs have only begun to appear recently and have been limited to exfoliated flakes of MoS_2[18−20] and WSe_2,[20] which were shown to exhibit the most stable and dominant, natural 2H layer stacking of their bulk parent crystals (Figure 1a). These studies showed that LF modes could

* Address correspondence to puretzkya@ornl.gov.

Received for review March 28, 2015 and accepted May 12, 2015.

Published online May 12, 2015
10.1021/acsnano.5b01884

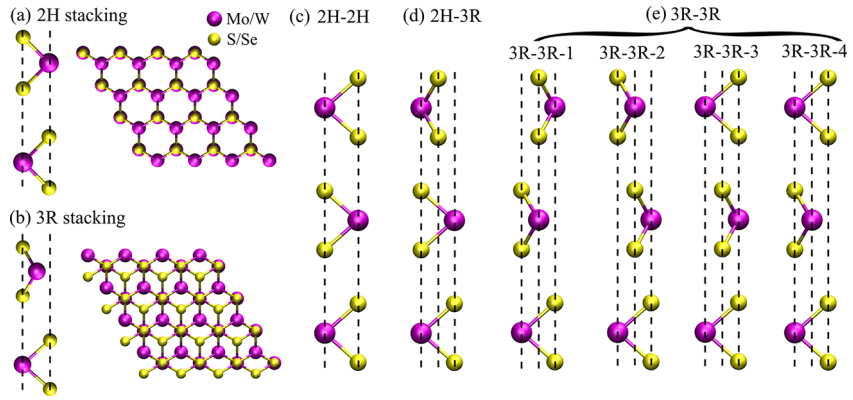

Figure 1. Side and top views of 2H and 3R stacking patterns of bilayer transition metal dichalcogenides MX_2, and side views of all possible combinations for trilayer MX_2. M stands for metal atom Mo or W, and X for chalcogen atom S or Se. Theoretical lattice constants and atomic coordinates of these stacking patterns for $MoSe_2$ are listed in section S4 in the Supporting Information. For bilayer, (a) 2H is the most stable stacking pattern (also named as AA′ stacking): M over X and X over M; (b) 3R is another common stacking (also named as AB stacking): M over X and the other M and X over the center of the hexagons. For trilayer, the possible stacking configurations include (c) 2H-2H, (d) 2H-3R, and (e) 3R-3R. Note that in (d) 2H-3R and 3R-2H are different stacking patterns if a substrate is involved. In (e), 3R-3R exhibits four different subpatterns marked as 3R-3R-1, 3R-3R-2, 3R-3R-3, and 3R-3R-4. The detailed explanation of these subpatterns is given in Figure S12 (Supporting Information).

be used to deterministically identify the number of layers in TMDs.[18−20] In addition to the dominant 2H stacking pattern, 3R stacking (Figure 1b) also appears in bulk and synthesized few-layer 2D TMD crystals.[21] Since the formation energy difference between these two stacking configurations is quite small (~1 meV/atom),[22,23] it is highly probable that these two phases will both be found in as-synthesized samples using for example, the most common chemical vapor deposition (CVD) approach. In addition to these most stable stacking configurations grown by CVD, an arbitrarily larger variety of TMD stacks can be produced by stamping their monolayers that create twisted multilayers with new properties.[22] This prompts a critical question: can Raman spectroscopy involving LF modes reveal distinguishing characteristics of 2D crystals that can serve as their unique fingerprints?

Here, we report measurements and *ab initio* calculations of LF Raman shear and breathing modes in CVD-synthesized bilayers (2L) of $MoSe_2$ and WSe_2 and trilayers (3L) of $MoSe_2$ on SiO_2/Si substrates. For the measured 2H and 3R stacking configurations for two-layers, and 2H-2H, 2H-3R, 3R-2H, 3R-3R stackings for three-layers, we show that each stacking configuration has a distinct characteristic LF Raman spectral fingerprint that can then be used for its unambiguous assignment. Differences between theory and experiment, discernible in these high-quality samples, are discussed.

RESULTS AND DISCUSSION

Low Frequency Raman Spectroscopy of 2L $MoSe_2$ and WSe_2. *2H versus 3R Stacking.* First, we examine the distinct LF Raman spectra of 2L $MoSe_2$ and WSe_2 for the most common stacking patterns (2H and 3R) formed during CVD synthesis on SiO_2/Si substrates as described in the Methods section.

2L $MoSe_2$. Figure 2a shows an optical microscope image of a large 1L triangular crystal of $MoSe_2$ decorated with five smaller triangular 1L crystals of the same material. Four of these smaller crystals are rotated at a 60° angle relative to the large 1L crystal and one (marked as number 3) shows a 0° rotation angle (see schematics in Supporting Information Figure S1b). According to recent studies on twisted bilayers of MoS_2,[22,24,25] the bilayers with a mutual rotation of 60° correspond to 2H stacking, while the ones with 0° rotation correspond to 3R stacking. As shown in Figure 1a, 2H (also denoted as AA′) stacking of bilayer $MoSe_2$ corresponds to Mo over Se and Se over Mo; in Figure 1b, 3R (also denoted as AB) stacking corresponds to Mo over Se and the other Mo and Se over the hexagon centers.[23,26] We will corroborate the stacking patterns below with direct atomic-resolution Z-contrast STEM microscopy measurements.

Figure 2b,c shows comparisons between the LF Raman spectra of the 2L $MoSe_2$ crystals measured at points 2 and 3 and the corresponding theoretical calculations (described in the Supporting Information Theory section). A complete set of the Stokes and anti-Stokes Raman spectra measured at all the points (1−6) is given in Figure S1. All Raman spectra that correspond to the bilayers with the mutual rotation of 60° (points 1, 2, 4, 5 in Figure 2a, 2H stacking) are identical (Figure S1), but the LF peaks measured for 0° rotation (*e.g.*, point 3, 3R stacking) are quite different from those measured for the 60° cases. The LF spectra (Figure 2b) show a narrow peak at 19.0 cm^{-1} (red line, 1.5 cm^{-1} full width half-maximum (fwhm)) and 18.5 cm^{-1} (blue line, 2 cm^{-1} fwhm) for the 2H and 3R stacking configurations, respectively, and a broad feature around 34 cm^{-1}. According to our *ab initio* calculations (Figure 2c and Supporting Information section S1, Figures S3a,b), these narrow peaks are assigned to

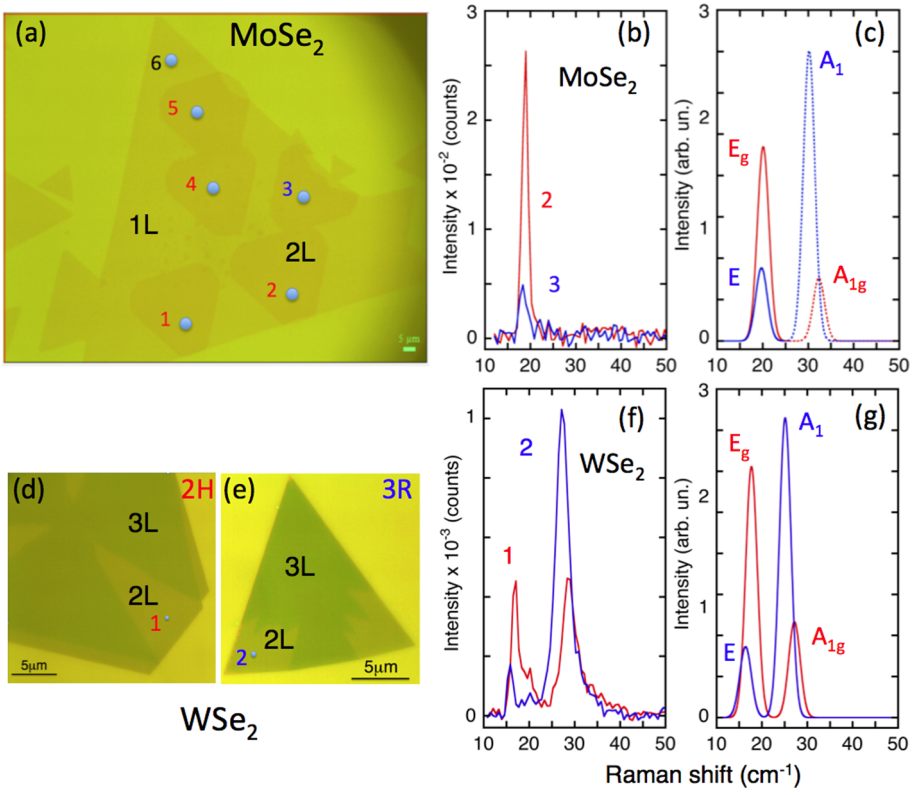

Figure 2. $MoSe_2$ and WSe_2 bilayer Raman spectra for 2H and 3R stacking patterns. All spectra were measured in $\bar{z}(x,x)z$ polarization configuration using the excitation laser power of ~0.3 mW ($\lambda = 532$ nm) and all samples were synthesized by CVD. (a) Optical microscope image of a large 1L $MoSe_2$ crystal decorated with 5 smaller 1L crystals to form 2L $MoSe_2$ with 0° (3R stacking, marked as 3) and 60° (2H stacking, marked as 1, 2, 4, 5) mutual rotations. (b) Low-frequency Raman spectra of 2L $MoSe_2$ for 2H (marked as 2) and 3R (marked as 3) stacking; the corresponding high-frequency Raman bands are shown in Figure S2b in Supporting Information. (c) Calculated LF Raman spectra for 2L $MoSe_2$ for 2H (red) and 3R (blue) stacking configurations. The dotted lines show the corresponding breathing modes that are very weak and broad in the experiment. (d and e) Optical microscope images of 2–3L WSe_2 crystals in 2H and 3R stacking configurations, respectively, for 2L. (f) Low-frequency Raman spectra of 2L WSe_2 for 2H (marked as 1) and 3R (marked as 2) stacking configurations, the corresponding high-frequency Raman bands are shown in Figure S2f of the Supporting Information. (g) Calculated LF Raman spectra for 2L WSe_2 for 2H (red) and 3R (blue) stacking configurations. All Raman spectra are shown with subtracted background.

the interlayer shear modes with the calculated frequencies of 20.1 cm^{-1} (E_g symmetry, 2H stacking) and 19.7 cm^{-1} (E symmetry, 3R stacking). The calculated interlayer breathing modes at 32.4 cm^{-1} (A_{1g}, 2H) and 30.2 cm^{-1} (A_1, 3R) correspond to the observed broad features at ~34 cm^{-1}. Note that the nomenclature changes for Raman modes for different stacking patterns are due to the change of symmetry, *i.e.*, different space and point groups (see more details in Figure S3 and section S1 in Supporting Information). Both experiment and theory show that the frequencies of the shear and breathing modes are slightly decreased from 2H to 3R stacking [~ 0.5 cm^{-1} (experiment) and ~0.4 cm^{-1} (theory) for the shear modes and ~2.2 cm^{-1} (theory) for the breathing mode], which is probably due to the slight weakening of the interlayer coupling for the 3R stacking configuration that is less energetically stable than 2H by ~1 meV/atom.[22,23] However, the most intriguing feature that can be easily used to distinguish these two stacking patterns for 2L $MoSe_2$, is the large drop (by a factor of 5.4) in the Raman intensity of the shear mode for 3R stacking (Figure 2b). More than the actual frequency values, this feature is the most effective way to distinguish these two stacking patterns for 2L $MoSe_2$. Our calculations also predict this intensity drop of the shear mode for 3R stacking configuration (by a factor of 2.7), a result that can be rationalized by the different symmetries of the 2D crystals in these stacking configurations (more details in section S1 in Supporting Information).

It is well-known that large variations in the quality of 2D TMDs (defects, impurities, *etc.*) exist depending on the synthesis method and even within same growth environment, for example, in the commonly used CVD approach. Therefore, there is a question about persistence of these characteristic changes in the LF Raman spectra for different stacking configurations: how do the Raman spectra of LF modes for the 2H and 3R stacking configurations depend on a synthesis method of these bilayer materials? To address this question, we conducted LF and HF Raman measurements using 2H and 3R bilayers of $MoSe_2$ that were exfoliated, grown by CVD, and grown by a combination of pulsed laser deposition (PLD) and CVD (see Methods).

Table S2 provides a summary of the measured frequencies of the LF shear and breathing modes and HF modes measured for 40 different 2H-stacked bilayers, and 32 different 3R-stacked bilayers synthesized in 8 different experiments (see Methods). We find that for 2H stacking the frequency of the shear mode varied from 19.0 ± 0.1 to 19.5 ± 0.1 cm^{-1} with the corresponding changes in the case of 3R stacking from 18.5 ± 0.2 to 19.1 ± 0.1 cm^{-1}. Despite these small variations in frequency in all experiments the shear mode for 3R-stacked bilayers was downshifted by 0.5 ± 0.1 cm^{-1} and a large drop in its intensity similar to that shown in Figure 2b was observed. In all these cases, including the exfoliated sample, the intensity of the breathing mode around 34.2 cm^{-1} was very low. Interestingly, similar to the case shown in Figure S2b the frequency of the HF mode (A_{1g} or A_1) remained unchanged for both 2H and 3R stacking configurations, although its absolute position varied from 242.0 ± 0.2 to 242.9 ± 0.2 cm^{-1} depending on a particular synthesis experiment.

The HF peak at 242.0 cm^{-1} (2.0 cm^{-1} fwhm) (Figure S2b) can be assigned to the A_{1g} out-of-plane vibrational mode in 2H stacking and to the A_1 mode in 3R stacking,[27,28] which is also confirmed by our calculations showing the HF peaks at 245.6 cm^{-1} (2H) and 245.8 cm^{-1} (3R) (Figure S2c). Interestingly, indiscernible changes in frequency and only modest changes in intensity are observed for the HF peak of 2L $MoSe_2$ (Figure S2b) for these 2H and 3R stackings. Therefore, the LF modes appear much more sensitive to the interlayer coupling and its variations for different layer stackings than the HF modes commonly used for Raman analysis of 2D crystals.

The extremely low intensity of the LF breathing mode observed in Figure 2b for 2L $MoSe_2$ with 2H stacking is not a common feature encountered in other TMDs. For example, in 2L MoS_2 a clear breathing mode around 40 cm^{-1} is observed for the 2H stacking configuration, however with approximately twice-lower intensity and significantly larger line width compared to that of the LF shear mode at 22 cm^{-1}.[20] However, our calculations did not quantitatively predict the observed intensities of the Raman bands in all the cases considered (including 2L $MoSe_2$ and 2L WSe_2 at both 2H and 3R stacking patterns, 3L $MoSe_2$ at 2H-2H, 2H-3R, 3R-2H, 3R-3R-1, 3R-3R-2, 3R-3R-3 and 3R-3R-4 stacking patterns, as will be discussed below). The most challenging case is 2L $MoSe_2$, where the interlayer breathing mode near 34 cm^{-1} is very weak and the corresponding Raman line is very broad and even undetectable in some cases. We note that there are a few possible mechanisms which can result in Raman line broadening of the breathing mode, such as anharmonic coupling with other low frequency modes (*e.g.*, acoustic modes)[29] and defects in the 2D crystals. However, we did not observe large amounts of defects in atomic resolution STEM. Also, our analysis of many different samples synthesized using different growth approaches (see Table S2 in Supporting Information) did not show any significant difference in the LF modes of 2L $MoSe_2$. Therefore, in this case it is unlikely that defects are responsible for the observed broadening and very low intensity of the LF breathing mode. Another possibility is related to the resonant Raman effect, which can strongly and selectively enhance Raman scattering for some specific modes through resonant electronic excitations. However, we also did not observe the LF breathing mode using 633 nm excitation. Thus, the most reasonable explanation of this effect is anharmonic coupling between different LF modes. The difference in the frequencies of the LF modes, their anharmonicities, and interlayer interactions could explain the strong coupling effect in the case of $MoSe_2$, but not for other TMDs.

Nevertheless, for 2L $MoSe_2$ and 2L WSe_2 with 2H and 3R stackings and 3L $MoSe_2$ with 2H-2H, 2H-3R, 3R-2H, 3R-3R stackings studied in this work, by considering only nonresonant Raman scattering of freestanding and defect-free 2D crystals using the harmonic approximation, *ab initio* calculations accurately predicted the measured phonon frequencies and provided qualitative agreements with the experimental Raman intensities and their stacking induced changes. Compared to Raman intensities that are sensitive to many external effects (laser wavelength, laser polarization, substrate, *etc.*), phonon frequencies are more intrinsic properties that can be predicted by our modeling of Raman spectra at very reasonable accuracy. However, the results also indicate that some important effects not considered in this modeling (such as anharmonic coupling between phonons or resonant Raman enhancement factors) can strongly affect the intensities of certain Raman modes.

2L WSe_2. Similar large differences in the relative intensities of the LF modes distinguished the 2H (Figure 2d) and 3R (Figure 2e) stacking patterns in 2L WSe_2. However, this time 2H stacking (red line in Figure 2f) yielded two equally intense peaks at 16.9 cm^{-1} (1.5 cm^{-1} fwhm) and 28.8 cm^{-1} (3.4 cm^{-1} fwhm) that correspond to the LF shear E_g and breathing A_{1g} modes, respectively. These two modes are very similar to those reported in ref 20 for exfoliated WSe_2, which also exhibited 2H stacking. For 3R stacking (blue line in Figure 2f), strong changes in the peak intensities of these two modes are observed, which are accompanied by small red shifts, *i.e.*, the intensity of the shear mode E that appears at 15.8 cm^{-1} (1.4 cm^{-1} fwhm) drops by a factor of 3.2, but the intensity of the breathing mode A_1 at 27.3 cm^{-1} (3.3 cm^{-1} fwhm) shows a large increase by a factor of 2.0 with red shifts of 1.1 and 1.5 cm^{-1}, respectively, compared to the corresponding 2H LF modes (red line in Figure 2f). Our calculated LF Raman spectra of 2L WSe_2 reproduce most

of the experimentally observed features (Figure 2g). First, from 2H to 3R stacking configurations, the LF shear and breathing modes are calculated to red shift by 1.3 and 2.1 cm^{-1}, respectively, in good agreement with the corresponding experimental values; second, the calculated intensity of the shear mode drops by a factor of ~3.5 while the calculated intensity of the breathing mode increases by a factor of ~3.1, confirming the measured intensity changes. Nonetheless, we note that the experimental intensity ratio between the shear and breathing modes fails to be precisely described by the calculations, particularly for 2H stacking (Figure 2f,g), since some important effects like anharmonic coupling between phonons and Raman resonance cannot be properly captured in our modeling of Raman spectra, as discussed above. The intensity ratio estimated by the model predictions is expected to accurately reflect the intrinsic value of a perfect system, however experimentally the ratio could be significantly altered due to anharmonic coupling of LF modes or selective Raman resonant enhancement of some specific modes.

The HF modes (A_{1g} for 2H and A_1 for 3R) of 2L WSe_2 do not show any relative shifts for these two stacking patterns, although for 3R stacking the HF peak intensity decreases by a factor of 2.0 compared to 2H stacking (Figure S2f). The corresponding Raman frequencies and intensities for the WSe_2 case are listed in Table S1, where the calculated frequencies and intensities are also shown for comparison (see also ref 30).

The large characteristic changes in the intensities of the LF modes, as well as their frequency shifts presented above, are clear fingerprints for fully determining a specific stacking configuration of 2L TMDs.

Combination of Atomic Resolution STEM and LF Raman Spectroscopy. *2L $MoSe_2$ Suspended on a TEM Grid.* To confirm these assignments of 2H and 3R stacking configurations in 2L $MoSe_2$ crystals, we performed measurements using atomic resolution STEM microscopy combined with Raman measurements performed at the same locations on a TEM grid (Figure S5). Figure 3 shows the Stokes and anti-Stokes Raman spectra measured at the same TEM grid positions used for the atomic resolution STEM measurements, confirming the assignments of 2H- and 3R-stackings (see also Figure S7). These Raman spectra and relative peak intensities are identical to those measured on SiO_2/Si substrates (see Figure 2a–c and Table S2): *i.e.*, the intensity of the shear mode at 18.7 ± 0.1 cm^{-1} in the case of 3R-stacking drops by a factor of 3.9 compared to that at 19.1 ± 0.1 cm^{-1} for the 2H-stacking with the corresponding red shift of 0.4 cm^{-1}. Note that for the suspended 2L $MoSe_2$ the damage threshold decreased ~3 times to 0.3 mW compared to the same 2D crystals on SiO_2/Si substrates, so the excitation laser power was reduced to 55 μW since (see Figures S4–S6, and section S2 in Supporting Information). This experiment

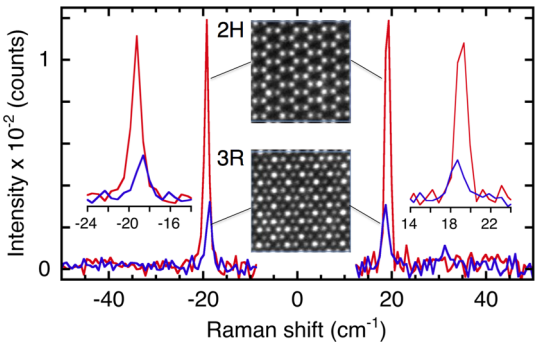

Figure 3. Raman spectra of 2L $MoSe_2$ measured on a TEM grid for 2H and 3R stacking patterns verified by atomic resolution STEM. Stokes (right) and anti-Stokes (left) LF Raman spectra of $MoSe_2$ bilayers suspended on a TEM grid. The insets show atomic resolution STEM images of the 2H (top) and 3R (bottom) stacking patterns taken at the locations used for the Raman measurements. The excitation laser power was 55 μW, acquisition time was 5 min.

confirms the feasibility of identifying the stacking patterns of 2D crystals based on their relative orientations measured by optical and AFM images.

Low Frequency Raman Spectroscopy of 3L $MoSe_2$ for Different Stacking Patterns. To understand if Raman spectroscopy can identify the atomic stacking registry in three-layer TMDs, we adjusted the CVD growth conditions to synthesize 3L $MoSe_2$ crystals in a variety of relative layer orientations (see Methods section). The six most stable, relaxed trilayer TMDs determined by our first-principles calculations can be categorized as the following bilayer combinations: 2H-2H, 2H-3R, and 3R-3R (see Figure 1c–e). Note that the relative shifts between metal or chalcogen atoms inherent in a 3R bilayer lead to four different 3R-3R stacking configuration subpatterns marked as 3R-3R-1, 3R-3R-2, 3R-3R-3, and 3R-3R-4 (Figure 1e and Figure S12). As we will show, the stacking patterns involving 2H stacking (with 60° relative orientation) can be identified from optical or AFM images for well-defined stacks of individual triangular crystals based on their relative orientations. However, the 3R-3R stacking subpatterns in 3L TMDs cannot be determined for crystals with 0° relative orientation without Raman spectroscopy.

Figure 4a–d shows a set of Raman spectra for LF and HF modes of 3L $MoSe_2$ together with the corresponding optical images of these structures (for additional information see Table S3 and Figure S8). These spectra clearly show that each stacking pattern has its own pronounced fingerprint in the LF Raman spectrum, *i.e.*, the 2H-2H stacking shows a narrow and intense peak at 24.0 ± 0.1 cm^{-1} (Figure 4a); the 2H-3R stacking with the 2H side laying on the SiO_2/Si substrate exhibits 2 peaks at 14.0 ± 0.1 and 23.4 ± 0.1 cm^{-1} (Figure 4b); the 3R-2H stacking with the 3R layers on the substrate shows exactly the same Raman spectra as for 2H-3R stacking (not shown in Figure 4, see Table S3); for the 3R-3R stacking, we found two

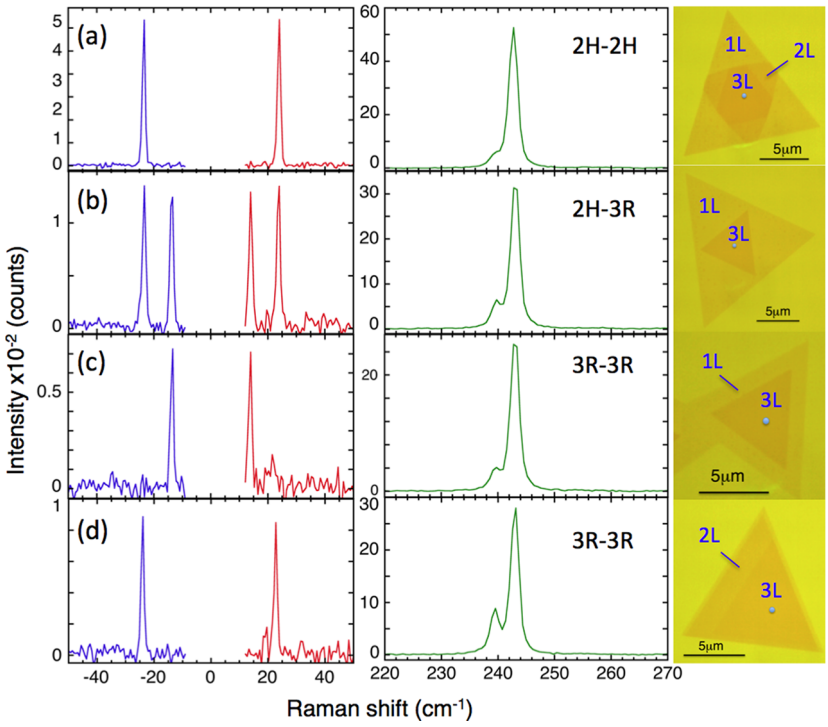

Figure 4. LF-Raman fingerprints of different stacking configurations in 3L $MoSe_2$. A set of Raman spectra for LF- and HF-modes of 3L $MoSe_2$ plotted together with the corresponding optical images of these structures (right). (a) 2H-2H, (b) 2H-3R, (c), (d) 3R-3R stacking configurations.

distinct types of Raman spectra with single peaks at 13.7 ± 0.1 cm^{-1} (Figure 4c) and 23.1 ± 0.2 cm^{-1} (Figure 4d), respectively. All these LF peaks are assigned to interlayer shear modes according to our laser polarized Raman measurements (described in detail in section S3 of the Supporting Information). By contrast, the HF Raman modes for 3L $MoSe_2$ did not exhibit similar discernible fingerprints like the LF modes, with nearly identical split peaks observed between 242.5 ± 0.2 to 243.0 ± 0.2 cm^{-1} and 239.3 ± 0.2 to 239.7 ± 0.2 cm^{-1}. These modes can be assigned to A'_1 or A_1 symmetries depending on the stacking (see Figures S3 and S9 for more details).

To explain the strong dependence of the measured LF shear mode spectra on stacking configuration for 3L $MoSe_2$ in Figure 4, we calculated Raman spectra for comparison, as shown in Figure S9. According to Figures S3 and S9, regardless of the stacking configuration, our calculations indicate two shear modes at ~13 and ~24 cm^{-1} (also see Table S3). The ~13 cm^{-1} shear modes in Figure S3 arise from vibration of the exterior layers in the trilayer, and thus show smaller restoring vdW forces and lower frequencies than the ~24 cm^{-1} mode that involves also the center layer. For 2H-2H (Figure S3c), 3R-3R-3 or 3R-3R-4 stacking (Figure S 3f), the lower-frequency shear mode around 13 cm^{-1} has symmetry E″ and its Raman tensor (see eq 3 in section S1 in Supporting Information) clearly shows that it has zero intensity, explaining why it was not observed in our experimental backscattering geometry. Therefore, only the higher-frequency shear mode E′ near 24 cm^{-1} appears in the calculated Raman spectra (Figure S9a,d) in agreement with the experimental spectra in Figure 4a,d. Thus, the only configurations with 3R-3R stacking and the proper symmetry to result in the single 24 cm^{-1} peak observed in Figure 4d must correspond to 3R-3R-3 or 3R-3R-4 stacking. For 2H-3R or 3R-2H (Figure S3d), and 3R-3R-1 or 3R-3R-2 stacking (Figure S3e), the system has lower symmetry, and the lower-frequency shear mode around 13 cm^{-1} switches to symmetry E with the Raman tensors described by eq 2 (section S1 in Supporting Information), the calculations now predicting that this 13 cm^{-1} peak should be observable in the backscattering geometry. In addition, for 2H-3R or 3R-2H stacking, the higher-frequency shear mode E near 24 cm^{-1} is also predicted to have nonzero intensity according to our calculations (Figure S9b). Consequently, the 2H-3R and 3R-2H stacking exhibit two peaks around 13 and 24 cm^{-1}, in agreement with the experimental Raman spectrum in Figure 4b. However, according to our calculations, although 3R-3R-1 or 3R-3R-2 stacking have the same symmetry and the shear mode E near 24 cm^{-1} is Raman-active, its Raman intensity is predicted to be very close to zero due to its extremely small Raman tensor (more details are given in Supporting Information section S1) and therefore should not be observable (Figure S9c). Therefore, 3R-3R-1 or 3R-3R-2 stacking should exhibit essentially only one Raman peak around 13 cm^{-1}, which is very consistent with the experimental Raman spectrum in

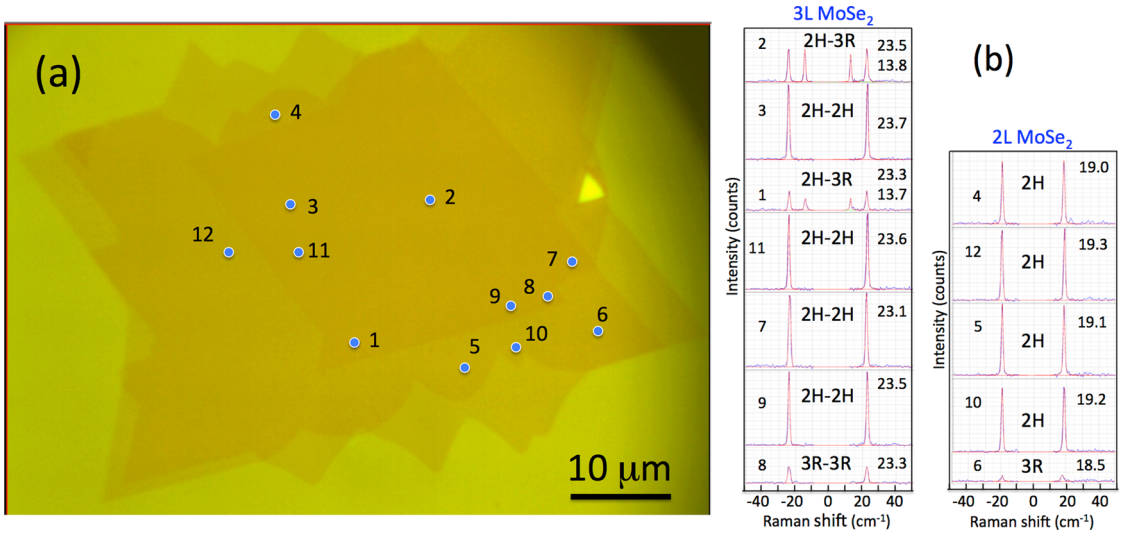

Figure 5. An example of decoding the number of layers and stacking configurations for a complex few layer structure of randomly stacked 2D $MoSe_2$ crystals synthesized by CVD. (a) The stacking configurations are measured for the points 1−12 marked with dots in the optical microscope image of this structure. (b) LF Raman (Stokes and anti-Stokes) spectra measured at the points 1−12 for a complex stacked $MoSe_2$ structure that were used to decode the number of layers and stacking configurations based on their fingerprints (Figures 2 and this figure). All spectra (blue lines) were measured in $\bar{z}(x,x)z$ polarization configuration and fit with a Gaussian−Lorentzian line-shape function (red lines) after background subtraction. The spectra are grouped into two columns based on the number of layers, 3L (left) and 2L (right). The numbers on the left of each column correspond to the positions of the dots in (a). The numbers on the right show the Raman frequencies in cm^{-1} obtained from the fitting. All the intensities in each column are scaled to the highest measured intensity of 453 counts for 3L (point 9) and 419 counts for 2L $MoSe_2$ (point 5). Note that the 3R-3R-3, 4 and 2H-2H stacking configurations with the same Raman frequencies were distinguished based on the considerable difference in the intensities of their Raman lines.

Figure 4c. Thus, for example, the 3R-3R stacking in Figure 4c can be categorically assigned to 3R-3R-1 or 3R-3R-2 stacking.

The stacking configurations can be determined simply based on the large difference in the ratio of the intensities of the LF shear and HF out-of-plane (242 cm^{-1}) modes, I_{LF}(shear)/I_{HF}(out-of-plane), without comparison between different stacking patterns of two or more 2D crystals. Table S4 (Supporting Information), shows the corresponding values of I_{LF}(shear)/I_{HF}(out-of-plane) of 2L $MoSe_2$ for all the experiments listed in Table S2. Similar stacking-sensitive intensity ratios for 3L $MoSe_2$ are listed in Table S5. For example, this ratio is 0.11 ± 0.02 for 2H and 0.019 ± 0.003 for 3R stacking configurations in the case of pure 2L $MoSe_2$ samples synthesized in different experiments described in the Methods section (see Table S4). Note that the parallel polarization configuration, $[\bar{z}(x,x)z]$, should be used for these measurements since the out-of-plane HF mode simply disappears under the perpendicular polarization configuration, $[\bar{z}(x,y)z]$. Another important point that should be considered in these measurements is the similarity in the dependences of I_{LF} and I_{HF} on the sample orientations. Although, the analysis of many crystals with random orientations within each experiment listed in Tables S4 and S5 indicates the independence of I_{LF}/I_{HF} on the crystal orientations, we verified this conclusion by direct measurements of I_{LF} and I_{HF} *versus* the sample rotation angle in the case of 2H-2H stacking of 3L $MoSe_2$ (Figure S11) and found the identical behavior of these intensities *versus* the rotation angles. Therefore, the intensity ratio is independent of the crystal orientation and its significant change can only be attributed to the stacking change.

In short, with coordinated experiment and theory, the LF Raman spectra can be used to categorically fingerprint the stacking configuration, even when such clearly discerned crystalline boundaries are not available as a guide of the stacking symmetry. For example, Figure 5 illustrates how the LF Raman modes can decode the number of layers and stacking configurations within complex, few-layer $MoSe_2$ structure using the fingerprints derived above.

CONCLUSIONS

In summary, we conclude that layers of 2D materials with different atomic registries have characteristic experimental Raman spectra fingerprints that are ultimately predictable by first-principles calculations. High resolution Raman spectroscopy of the relatively perfect 2D bilayers and trilayers synthesized by our CVD allow differences between experimental and calculated spectra to be observed, and highlight the need for further improvements in theory. For example, the use of the harmonic approximation and the assumption of nonresonant Raman scattering in the current model could not accurately describe the line widths of the LF shear and breathing modes, as revealed by the experimental spectra showing broader Raman lines for

the LF breathing modes. In addition, the broad and very weak LF breathing mode in the case of 2L $MoSe_2$ may reflect the need to include anharmonic coupling with other LF modes including acoustic ones. Calculations are currently in progress to more rigorously quantify and investigate the role of anharmonicity. Extremely high quality few-layer 2D TMD crystals that are atomistically and computationally tractable are essential test-beds to fully develop theoretical and computational refinements. Notwithstanding these future improvements, it is clear that LF Raman spectra and first-principles modeling provide a simple and effective approach for the precise characterization of the stacking configurations in 2D TMDs, providing an efficient, nondestructive rapid and remote optical method to accelerate the characterization of 2D heterostructures in this rapidly developing field.

METHODS

Sample Preparation. 2D $MoSe_2$ (experiments 1, 2, see Table S2) and W doped $MoSe_2$ (experiments 3, 6) crystals were synthesized by CVD using a tube furnace setup equipped with a 2-in. quartz tube at growth temperature of 780 °C. In a typical run, the growth substrates, Si with 250 nm SiO_2 (SiO_2/Si), were cleaned with acetone and isopropyl alcohol and were placed face-down above an alumina crucible containing ~0.25 g of MoO_3 powder (in the case of W doped $MoSe_2$, a mixture of ~0.2 g MoO_3 and ~0.2 g WO_3 powder was used), which was then inserted into the center of the quartz tube. Another crucible containing ~1.2 g Se powder was located at the upstream side of the tube. After evacuating the tube to ~5 mTorr, flows of 40 sccm (standard cubic centimeter per minute) argon and 4 sccm hydrogen gas were introduced into the tube, and the reaction was conducted at 780 °C (with a ramping rate of 30 °C/min) for 10 min at the total pressure of 20 Torr. At 780 °C, the temperature at the location of Se powder was ~290 °C. After growth, the furnace was cooled naturally to room temperature.

In experiments 5 and 7, the 2D $MoSe_2$ crystals were synthesized in our second CVD setup, which also used a 2-in. quartz tube mounted in a horizontal tube furnace and MoO_3 and Se powders as feedstock, but at slightly higher growth temperature of 800 °C. In this case, 0.3 g MoO_3 and 0.5 g Se powders were placed at the center of the heating zone and upstream at the point with $T \sim 300$ °C, respectively. After consecutive cleaning by acetone, isopropyl alcohol, and deionized water, the growth substrates were faced down and placed above the crucible containing MoO_3 powder in the center of the heating zone. Then the furnace was heated up to 800 °C in 30 min and maintained at this temperature for 10 min with a constant flow of 40 sccm Ar and 5 sccm H_2 at the total pressure of 10 Torr and finally cooled down to room temperature.

2D crystals of WSe_2 were synthesized using Ar/H_2 (8:1) at 760 Torr in the second CVD setup described above at growth temperature of 850 °C. Similarly, two alumina crucibles loaded with WO_3 powder and Se pellets were positioned in the center of the furnace and upstream, respectively. SiO_2/Si substrates were placed in close proximity to WO_3 crucible at the downstream side. First, the temperature was ramped up to 550 °C and kept for 10 min with 100 sccm Ar/H_2 flow, then it was increased to 850 °C at 15 °C/min with the gas flow reduced to 40 sccm gas flow and kept at these conditions for 30 min, and then cool down naturally with 200 sccm gas flow.

To synthesize 2D $MoSe_2$ crystals in the experiment 4, the PLD/CVD approach was employed, which was described in detail in ref 31. Briefly, stoichiometric $MoSe_2$ nanoparticles were first synthesized and deposited onto a SiO_2/Si substrate by pulsed laser deposition (PLD) at room temperature in Ar background gas. Then, this source substrate was covered with a receiver (SiO_2/Si) substrate to form a confined CVD system with a temperature gradient between a hotter source substrate, which was in direct contact with a heater surface kept at 950 °C and a cooler receiver substrate.

Note that to synthesize perfect 2L and 3L $MoSe_2$ crystals in order to identify their stacking configurations based on optical and AFM images in some cases we added a very small amount of WO_3 to the other CVD precursors. This procedure causes only minor doping (~1−3%) of the synthesized 2D $MoSe_2$ crystals according to our atomic resolution STEM measurements for 2L case (bright dots in Figure S7a), but did not lead to any measurable differences in the Raman spectra compared to undoped materials (see Table S2).

Samples Characterization. The number of layers in the 2D crystals was determined using atomic force microscopy (AFM) (Bruker Dimension Icon AFM). The ADF-STEM images were obtained using an aberration-corrected Nion UltraSTEM operating at 100 kV. To prepare the TEM samples, we first spun Poly Methyl Methacrylate (PMMA) onto a SiO_2/Si substrate with 2D crystals at 3500 rpm for 60 s. The PMMA-coated substrate was then put in 1 M KOH solution that etched silica epi-layer, leaving the PMMA film with the 2D crystals floating on the liquid surface. The films were transferred to deionized water to remove residual KOH and then scooped onto a Si TEM grid covered by 50 nm-thick amorphous SiN film with 2 μm openings. The PMMA was removed by acetone followed by baking at 300 °C under ~30 Torr of flowing Ar/H_2 (0.95/0.05).

Raman Measurements. Raman spectra were acquired using a micro-Raman system based on a Jobin-Yvon T64000 triple spectrometer consisting of a double monochromator (in dispersion subtractive mode) coupled to a third spectrometer stage with 1800 grooves per millimeter gratings (spectral resolution ~0.7 cm^{-1}, fwhm) and equipped with a liquid nitrogen cooled CCD detector (Symphony Horiba JY). All measurements were performed at room temperature under a microscope in backscattering configuration using a 532 nm continuous wave solid-state laser. The laser light was focused on a sample surface by a 100× objective (N/A = 0.9) with a spot size of ~1 μm. The excitation laser power on the samples was ~0.3 mW for 2D crystals on SiO_2/Si substrates and was reduced to 55 μW for measurements on TEM grids. The acquisition time was adjusted to get a sufficient signal-to-noise ratio and was varied from 20 s for the most experiments to 5 min for the experiments on TEM grids. Note that 3 gratings in the triple-monochromator selected only $\bar{z}(x,x)z$ polarization configuration; therefore, all measurements except the polarized ones described in section S3 in Supporting Information were performed in parallel polarization configuration without using a polarizer in the scattered beam. To perform polarized Raman measurements, a polarizer and a half-wave plate were inserted into the scattered beam path to get $\bar{z}(x,x)z$ or $\bar{z}(x,y)z$ polarization configurations and to rotate the scattered light polarization to satisfy the grating's polarization requirements. To measure the polarization angle dependences, the polarization of the incident laser light was fixed and the samples were rotated around the laser spot.

Theoretical Methods. Plane-wave density functional theory (DFT) calculations were performed using the VASP package[32] equipped with the projector augmented-wave (PAW) method for electron−ion interactions. Local density approximation (LDA) has been shown to yield excellent description of electron and phonon properties of 2D TMDs.[20,22,24,33] Hence, LDA was adopted for the exchange-correlation interaction with the energy cutoff set at 400 eV. For bulk $MoSe_2$ and WSe_2, both atoms and cell volumes were allowed to relax until the residual forces were below 0.001 eV/Å. We used a 24 × 24 × 4 k-point sampling in the Monkhorst−Pack scheme.[34] The optimized lattice parameters of $MoSe_2$ (WSe_2) are a = 3.25 (3.25) and

c = 12.69 (12.75) Å. Note that the differences between lattice parameters of 2H and 3R stacking are very small and negligible. Then, 2L and 3L systems at various stacking configurations were modeled by a periodic slab geometry using the optimized in-plane lattice constants of the bulk. A vacuum region of at least 18 Å in the z direction normal to the plane was used to avoid spurious interactions with replicas. For the 2D slab calculations, all atoms were relaxed until the residual forces were below 0.001 eV/Å and 24 × 24 × 1 k-point samplings were used.

Nonresonant Raman calculations were performed using the fully relaxed geometries. Since the Raman intensity $I \propto |e_i \cdot \alpha \cdot e_s|^2$, the calculations of the Raman tensors α are most important. This requires information on the phonon frequencies, phonon eigenvectors (*i.e.*, vibrations) and the changes of the polarizability or dielectric constant tensors with respect to phonon vibrations (see more details and equations in ref 33). To obtain Raman scattering, one needs to calculate the dynamic matrix and derivatives of the dielectric constant tensors. The dynamic matrix was calculated using the *ab initio* direct method,[35] implemented in the PHONON software.[36] In the finite difference scheme,[37] the Hellmann−Feynman forces in the supercell were computed by VASP for both positive and negative atomic displacements (δ = 0.03 Å) and used in PHONON to construct the dynamic matrix, whose diagonalization provides phonon frequencies and eigenvectors. The derivatives of the dielectric constant tensor were also calculated by the finite difference approach. For both positive and negative atomic displacements in the single unit cell, the dielectric tensors were computed by VASP using density functional perturbation theory and then imported into PHONON to generate their derivatives. From this, the Raman intensity for every phonon mode was obtained for a given laser polarization setup and wavelength to finally yield a Raman spectrum after Gaussian broadening.

Conflict of Interest: The authors declare no competing financial interest.

Acknowledgment. Raman spectroscopy part of this research was conducted at the Center for Nanophase Materials Sciences, which is sponsored at Oak Ridge National Laboratory by the Scientific User Facilities Division, Office of Basic Energy Sciences, U.S. Department of Energy. Synthesis science, including CVD and PLD, was supported by the U.S. Department of Energy, Office of Science, Basic Energy Sciences, Materials Sciences and Engineering Division. The theoretical work at Rensselaer Polytechnic Institute (RPI) was supported by New York State under NYSTAR program C080117 and the Office of Naval Research. The computations were performed using the resources of the Center for Computational Innovation at RPI. L.B. acknowledges the financial support of the National Secretariat of Higher Education, Science, Technology and Innovation of Ecuador (SENESCYT).

Supporting Information Available: Schematic of 2L $MoSe_2$ crystal orientations and corresponding Raman spectra; calculated vibrational patterns, selection rules, and LF Raman frequencies; group theory analysis and first-principle calculations; tables of experimental and calculated Raman frequencies and peak intensities; effects of laser power; atomic resolution STEM measurements; AFM images; calculated LF Raman spectra for 3L $MoSe_2$; polarized Raman measurements; schematics of four 3R-3R subpatterns; theoretical lattice constants and atomic coordinates of studied $MoSe_2$ stacking patterns. The Supporting Information is available free of charge on the ACS Publications website at DOI: 10.1021/acsnano.5b01884.

REFERENCES AND NOTES

1. Novoselov, K. S. Nobel Lecture: Graphene: Materials in the Flatland. *Rev. Mod. Phys.* **2011**, *83*, 837–849.
2. Butler, S. Z.; Hollen, S. M.; Cao, L. Y.; Cui, Y.; Gupta, J. A.; Gutierrez, H. R.; Heinz, T. F.; Hong, S. S.; Huang, J. X.; Ismach, A. F.; et al. Progress, Challenges, and Opportunities in Two-Dimensional Materials beyond Graphene. *ACS Nano* **2013**, *7*, 2898–2926.
3. Geim, A. K.; Grigorieva, I. V. Van der Waals Heterostructures. *Nature* **2013**, *499*, 419–425.
4. Huang, C.; Wu, S.; Sanchez, A. M.; Peters, J. J. P.; Beanland, R.; Ross, J. S.; Rivera, P.; Yao, W.; Cobden, D. H.; Xu, X. Lateral Heterojunctions within Monolayer $MoSe_2$−WSe_2 Semiconductors. *Nat. Mater.* **2014**, *13*, 1096–1101.
5. Gong, Y.; Lin, J.; Wang, X.; Shi, G.; Lei, S.; Lin, Z.; Zou, X.; Ye, G.; Vajtai, R.; Yakobson, B. I.; et al. Vertical and in-Plane Heterostructures from WS_2/MoS_2 Monolayers. *Nat. Mater.* **2014**, *13*, 1135–1142.
6. Britnell, L.; Ribeiro, R. M.; Eckmann, A.; Jalil, R.; Belle, B. D.; Mishchenko, A.; Kim, Y. J.; Gorbachev, R. V.; Georgiou, T.; Morozov, S. V.; et al. Strong Light-Matter Interactions in Heterostructures of Atomically Thin Films. *Science* **2013**, *340*, 1311–1314.
7. Hong, X. P.; Kim, J.; Shi, S. F.; Zhang, Y.; Jin, C. H.; Sun, Y. H.; Tongay, S.; Wu, J. Q.; Zhang, Y. F.; Wang, F. Ultrafast Charge Transfer in Atomically Thin MoS_2/WS_2 Heterostructures. *Nat. Nanotechnol.* **2014**, *9*, 682–686.
8. Yu, W. J.; Liu, Y.; Zhou, H. L.; Yin, A. X.; Li, Z.; Huang, Y.; Duan, X. F. Highly Efficient Gate-Tunable Photocurrent Generation in Vertical Heterostructures of Layered Materials. *Nat. Nanotechnol.* **2013**, *8*, 952–958.
9. Dresselhaus, M. S.; Dresselhaus, G.; Saito, R.; Jorio, A. Raman Spectroscopy of Carbon Nanotubes. *Phys. Rep.* **2005**, *409*, 47–99.
10. Dresselhaus, M. S.; Dresselhaus, G.; Jorio, A. Raman Spectroscopy of Carbon Nanotubes in 1997 and 2007. *J. Phys. Chem. C* **2007**, *111*, 17887–17893.
11. Dresselhaus, M. S.; Dresselhaus, G.; Hofmann, M. The Big Picture of Raman Scattering in Carbon Nanotubes. *Vib. Spectrosc.* **2007**, *45*, 71–81.
12. Ferrari, A. C.; Meyer, J. C.; Scardaci, V.; Casiraghi, C.; Lazzeri, M.; Mauri, F.; Piscanec, S.; Jiang, D.; Novoselov, K. S.; Roth, S.; et al. Raman Spectrum of Graphene and Graphene Layers. *Phys. Rev. Lett.* **2006**, *97*, 187401.
13. Dresselhaus, M. S.; Dresselhaus, G.; Hofmann, M. Raman Spectroscopy as a Probe of Graphene and Carbon Nanotubes. *Philos. Trans. R. Soc., A* **2008**, *366*, 231–236.
14. Saito, R.; Hofmann, M.; Dresselhaus, G.; Jorio, A.; Dresselhaus, M. S. Raman Spectroscopy of Graphene and Carbon Nanotubes. *Adv. Phys.* **2011**, *60*, 413–550.
15. Zhang, X.; Qiao, X.-F.; Shi, W.; Wu, J.-B.; Jiang, D.-S.; Tan, P.-H. Phonon and Raman Scattering of Two-Dimensional Transition Metal Dichalcogenides from Monolayer, Multilayer to Bulk Material. *Chem. Soc. Rev.* **2015**, *44*, 2757–2785.
16. Tan, P. H.; Han, W. P.; Zhao, W. J.; Wu, Z. H.; Chang, K.; Wang, H.; Wang, Y. F.; Bonini, N.; Marzari, N.; Pugno, N.; et al. The Shear Mode of Multilayer Graphene. *Nat. Mater.* **2012**, *11*, 294–300.
17. Wu, J.-B.; Zhang, X.; Ijas, M.; Han, W. P.; Qiao, X.-F.; Li, X.-L.; Jiang, D.-S.; Ferrari, A. C.; Tan, P.-H. Resonant Raman Spectroscopy of Twisted Multilayer Graphene. *Nat. Commun.* **2014**, *5*, 5309.
18. Zeng, H. L.; Zhu, B. R.; Liu, K.; Fan, J. H.; Cui, X. D.; Zhang, Q. M. Low-Frequency Raman Modes and Electronic Excitations in Atomically Thin MoS_2 Films. *Phys. Rev. B* **2012**, *86*, 241301(R).
19. Zhang, X.; Han, W. P.; Wu, J. B.; Milana, S.; Lu, Y.; Li, Q. Q.; Ferrari, A. C.; Tan, P. H. Raman Spectroscopy of Shear and Layer Breathing Modes in Multilayer MoS_2. *Phys. Rev. B* **2013**, *87*, 115413.
20. Zhao, Y. Y.; Luo, X.; Li, H.; Zhang, J.; Araujo, P. T.; Gan, C. K.; Wu, J.; Zhang, H.; Quek, S. Y.; Dresselhaus, M. S.; et al. Inter Layer Breathing and Shear Modes in Few-Trilayer MoS_2 and WSe_2. *Nano Lett.* **2013**, *13*, 1007–1015.
21. Wang, S.; Zhang, J.; He, D.; Zhang, Y.; Wang, L.; Xu, H.; Wen, X.; Ge, H.; Zhao, Y. Sulfur-Catalyzed Phase Transition in MoS_2 under High Pressure and Temperature. *J. Phys. Chem. Solids* **2014**, *75*, 100–104.
22. Huang, S. X.; Ling, X.; Liang, L. B.; Kong, J.; Terrones, H.; Meunier, V.; Dresselhaus, M. S. Probing the Interlayer Coupling of Twisted Bilayer MoS_2 Using Photoluminescence Spectroscopy. *Nano Lett.* **2014**, *14*, 5500–5508.
23. He, J. G.; Hummer, K.; Franchini, C. Stacking Effects on the Electronic and Optical Properties of Bilayer Transition

Metal Dichalcogenides MoS_2, $MoSe_2$, WS_2, and WSe_2. *Phys. Rev. B* **2014**, *89*, 075409.
24. Van der Zande, A. M.; Kunstrnann, J.; Chernikov, A.; Chenet, D. A.; You, Y. M.; Zhang, X. X.; Huang, P. Y.; Berkelbach, T. C.; Wang, L.; Zhang, F.; et al. Tailoring the Electronic Structure in Bilayer Molybdenum Disulfide *via* Interlayer Twist. *Nano Lett.* **2014**, *14*, 3869–3875.
25. Liu, K. H.; Zhang, L. M.; Cao, T.; Jin, C. H.; Qiu, D. A.; Zhou, Q.; Zettl, A.; Yang, P. D.; Louie, S. G.; Wang, F. Evolution of Interlayer Coupling in Twisted Molybdenum Disulfide Bilayers. *Nat. Commun.* **2014**, *5*, 5966.
26. Constantinescu, G.; Kuc, A.; Heine, T. Stacking in Bulk and Bilayer Hexagonal Boron Nitride. *Phys. Rev. Lett.* **2013**, *111*, 036104.
27. Terrones, H.; Del Corro, E.; Feng, S.; Poumirol, J. M.; Rhodes, D.; Smirnov, D.; Pradhan, N. R.; Lin, Z.; Nguyen, M. A. T.; Elias, A. L.; et al. New First Order Raman-Active Modes in Few Layered Transition Metal Dichalcogenides. *Sci. Rep.* **2014**, *4*, 4215.
28. Tonndorf, P.; Schmidt, R.; Bottger, P.; Zhang, X.; Borner, J.; Liebig, A.; Albrecht, M.; Kloc, C.; Gordan, O.; Zahn, D. R. T.; et al. Photoluminescence Emission and Raman Response of Monolayer MoS_2, $MoSe_2$, and WSe_2. *Opt. Express* **2013**, *21*, 4908–4916.
29. Boukhicha, M.; Calandra, M.; Measson, M. A.; Lancry, O.; Shukla, A. Anharmonic Phonons in Few-layer MoS_2: Raman Spectroscopy of Ultralow Energy Compression and Shear Modes. *Phys. Rev. B* **2013**, *87*, 195316.
30. Luo, X.; Zhao, Y.; Zhang, J.; Toh, M.; Kloc, C.; Xiong, Q.; Quek, S. Y. Effects of Lower Symmetry and Dimensionality on Raman Spectra in Two-Dimensional WSe_2. *Phys. Rev. B* **2013**, *88*, 195313.
31. Mahjouri-Samani, M.; Tian, M.; Wang, K.; Boulesbaa, A.; Rouleau, C. M.; Puretzky, A. A.; McGuire, M. A.; Srijanto, B. R.; Xiao, K.; Eres, G.; et al. Digital Transfer Growth of Patterned 2D Metal Chalcogenides by Confined Nanoparticle Evaporation. *ACS Nano* **2014**, *8*, 11567–11575.
32. Kresse, G.; Furthmuller, J. Efficiency of Ab-Initio Total Energy Calculations for Metals and Semiconductors Using a Plane-Wave Basis Set. *Comput. Mater. Sci.* **1996**, *6*, 15–50.
33. Liang, L. B.; Meunier, V. First-Principles Raman Spectra of MoS_2, WS_2 and Their Heterostructures. *Nanoscale* **2014**, *6*, 5394–5401.
34. Monkhorst, H. J.; Pack, J. D. Special Points for Brillouin-Zone Integrations. *Phys. Rev. B* **1976**, *13*, 5188–5192.
35. Parlinski, K.; Li, Z. Q.; Kawazoe, Y. First-Principles Determination of the Soft Mode in Cubic ZrO_2. *Phys. Rev. Lett.* **1997**, *78*, 4063–4066.
36. Parlinski, K. *Computer Code PHONON*; Krakow, Poland, 2010.
37. Liang, L. B.; Meunier, V. Electronic and Thermoelectric Properties of Assembled Graphene Nanoribbons with Elastic Strain and Structural Dislocation. *Appl. Phys. Lett.* **2013**, *102*, 143101.